Journal of Computational Physics 228 (2009) 5000–5019

Contents lists available at ScienceDirect

Journal of Computational Physics

journal homepage: www.elsevier.com/locate/jcp

The adaptive immersed interface finite element method for elliptic and Maxwell interface problems

Zhiming Chen [a,*,1], Yuanming Xiao [b], Linbo Zhang [a,2]

[a] LSEC, Institute of Computational Mathematics, Academy of Mathematics and Systems Science, Chinese Academy of Sciences, Beijing 100080, People's Republic of China
[b] Department of Mathematics, Nanjing University, Nanjing 210093, People's Republic of China

ARTICLE INFO

Article history:
Received 22 November 2008
Received in revised form 16 March 2009
Accepted 21 March 2009
Available online 3 May 2009

Keywords:
Adaptive finite element method
Interface problems
Non-body-fitted meshes
Elliptic equation
Maxwell's equations

ABSTRACT

We propose self-adaptive finite element methods with error control for solving elliptic and electromagnetic problems with discontinuous coefficients. The meshes in the methods do not need to fit the interfaces. New error indicators are introduced to control the error due to non-body-fitted meshes. Flexible *h*-adaptive strategies are developed, which can be systematically extended to a large class of interface problems. Extensive numerical experiments are performed to support the theoretical results and to show the competitive behavior of the adaptive algorithm even for interfaces involving corner or tip singularities.

1. Introduction

The interface problems which involve partial differential equations having discontinuous coefficients across certain interfaces are often encountered in fluid dynamics, electromagnetics, and materials science. Because of the low global regularity and the irregular geometry of the interface, the standard numerical methods which are efficient for smooth solutions usually lead to loss in accuracy across the interface. Let Ω be a bounded domain in $\mathbb{R}^d$ $(d = 2, 3)$ which is divided into two subdomains Ω_1, Ω_2 by some surface $\Gamma = \overline{\Omega}_1 \cap \overline{\Omega}_2$. One of the model problems we will consider in this paper is the following elliptic problem

$$-\mathrm{div}(a(x)\nabla u) = f \quad \text{in } \Omega_1 \cup \Omega_2, \quad u = 0 \quad \text{on } \partial\Omega \tag{1}$$

with homogeneous jump conditions across the interface Γ

$$[\![u]\!]_\Gamma = 0, \quad \left[\!\left[a(x)\frac{\partial u}{\partial \mathbf{n}}\right]\!\right]_\Gamma = 0 \quad \text{on } \Gamma. \tag{2}$$

* Corresponding author.
E-mail addresses: zmchen@lsec.cc.ac.cn (Z. Chen), xym@nju.edu.cn (Y. Xiao), zlb@lsec.cc.ac.cn (L. Zhang).

[1] This author was supported in part by China NSF under the grant 10428105 and by the National Basic Research Project under the grant 2005CB321701.
[2] This author was supported in part by China NSF under the grants 10531080 and 60873177, and by the National Basic Research Project under the grant 2005CB321702.

0021-9991/$ - see front matter © 2009 Elsevier Inc. All rights reserved.
doi:10.1016/j.jcp.2009.03.044

Here $[[v]]_\Gamma$ stands for the jump of a quantity v across the interface Γ and $\mathbf{n}$ denotes the unit outer normal to the boundary of one subdomain, say $\partial\Omega_1$. Across the interface Γ, the coefficient function $a(x)$ is discontinuous. For simplicity we assume in this paper $a(x) = a_i$ in Ω_i for positive constant a_i, $i = 1, 2$.

For arbitrarily shaped interface Γ, it is known that optimal or nearly optimal convergence rate can be achieved if body-fitted finite element meshes are used, see e.g. [1,8]. In a body-fitted mesh, the sides (2D) or the edges (3D) intersect with the interface only through the vertices, see Fig. 1. Unfortunately, it is usually a nontrivial and time-consuming task to construct good body-fitted meshes for problems involving geometrically complicated interfaces. Therefore, numerous modified finite difference methods based only on simple Cartesian grids have been proposed in the literature. We refer to the immersed boundary method in Peskin [20], the immersed interface method in LeVeque and Li [15], Li and Ito [16], the ghost fluid method in Liu et al. [18], and the references therein. In Li et al. [17], an immersed interface finite element method is developed by a local modification of finite element basis functions.

While most of the aforementioned methods assume that the underlying solutions are smooth in each subdomain, they are not easily applied to problems involving non-smooth interfaces. Numerical solutions to this class of problems are challenging in science and engineering applications. It is well-known that the regularity of the solution for interface problems strongly depends on the geometry of the interface and discontinuity of the coefficients in the equation. For 2D elliptic interface problems, an exact solution was constructed by Kellog [14] which is in Sobolev space $H^{1+\delta}$, $\delta > 0$. The solution of Maxwell interface problems can have much stronger singularities which can be as bad as H^δ with $\delta < 1/2$, see e.g. [11].

The purpose of this paper is to develop an adaptive immersed interface finite element method (AIIFEM) for solving elliptic and Maxwell interface problems with singularity. The method extends the general idea of the adaptive finite element method based on a posteriori error estimates initiated in Babuška and Rheinboldt [3]. A posteriori error estimates are computable quantities in terms of the discrete solution and data that measure the actual discrete errors without the knowledge of exact solutions. The local contributions to the a posteriori error estimates can be used in designing adaptive algorithms for mesh modification based on the principle of error equi-distribution. For the a posteriori error estimation and the development of adaptive algorithms for interface problems having polygonal or polyhedral interfaces we refer to Chen and Dai [7] for elliptic problems and Chen et al. [9] for Maxwell cavity problems.

In this paper we assume the interface can be of arbitrary shape and the finite element mesh whose vertices are not necessarily located on the interface. The layout of this paper is as follows. In Section 2, we consider the 2D elliptic interface problem on an immersed finite element mesh and derive the a posteriori error estimate which takes into account the error due to non-body-fitted meshes. An efficient adaptive strategy is proposed and numerical examples are given to show the competitive behavior of the method. In Section 3, we consider the elliptic problem in 3D. In this case the straightforward extension of the method for 2D case in Section 2 fails. We introduce new finite element basis functions for the elements having non-empty intersection with the interface and obtain an AIIFEM which is quasi-optimal in the sense that the energy error decays as $CN^{-1/3}$, where N is the number of degrees of freedom. The proposed framework of AIIFEM method is then applied to solve Maxwell interface problems in Section 4.

2. The 2D elliptic interface problem

Let Ω be a polygonal domain in $\mathbb{R}^2$ with boundary Σ. For each integer $m \geqslant 0$ and real p with $1 \leqslant p \leqslant \infty$, $W^{m,p}(\Omega)$ denotes the standard Sobolev space of real scalar functions with their weak derivatives of order up to m in the Lebesgue space $L^p(\Omega)$. When $p = 2$, we use $H^m(\Omega)$ to stand for $W^{m,2}(\Omega)$.

Given $f \in L^2(\Omega)$, the weak formulation of (1) and (2) is to find $u \in H_0^1(\Omega)$ such that

$$a(u, v) = \int_\Omega f v \, dx \quad \forall v \in H_0^1(\Omega), \tag{3}$$

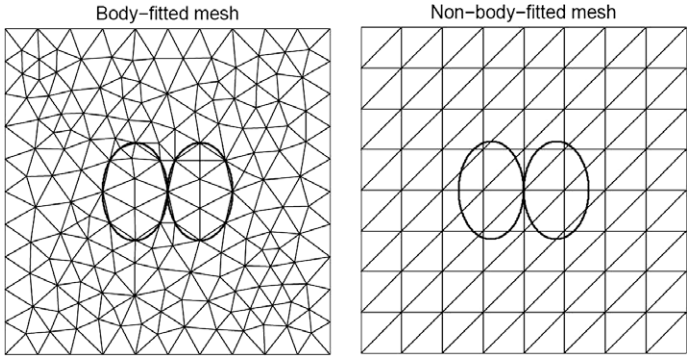

Fig. 1. The body-fitted and non-body-fitted mesh in 2D.

where

$$a(u,v) := \int_\Omega a(x)\nabla u \cdot \nabla v \,\mathrm{d}x \quad \forall u, v \in H^1(\Omega).$$

Let $\mathcal{M}_h$ be a regular triangular partition of the domain Ω. V_h denotes the standard H^1-conforming linear finite element space over the mesh $\mathcal{M}_h$

$$V_h = \{v_h \in H^1(\Omega) : v_h|_K \in P_1(K),\ \forall K \in \mathcal{M}_h\},$$

where $P_1(K)$ is the set of linear polynomials on K. Set $V_h^0 = V_h \cap H_0^1(\Omega)$. We call an element $K \in \mathcal{M}_h$ an interface element if the interface passes through the interior of K; otherwise we call K a non-interface element. The set of all interface elements is denoted by $\mathcal{M}_h^*$.

In order to approximate the weak problem (3), we need to define a discrete coefficient function $a_h(x)$. For the 2D problem, we take $a_h(x)$ as elementwise constant: $a_h(x) = a_K$ for $K \in \mathcal{M}_h$. For the non-interface element $K \in \mathcal{M}_h \setminus \mathcal{M}_h^*$, we set $a_K = a(x)$. For the interface element, we define a_K as either one of the two values a_1 or a_2. For definiteness, we set in the following

$$a_K = \min_{x\in K} a(x) \quad \forall K \in \mathcal{M}_h^*.$$

The discrete version of (3) is to find $u_h \in V_h^0$ such that

$$\int_\Omega a_h(x)\nabla u_h \cdot \nabla v_h \,\mathrm{d}x = \int_\Omega f v_h \,\mathrm{d}x \quad \forall v_h \in V_h^0. \tag{4}$$

By Lax–Milgram Lemma, (4) has a unique solution $u_h \in V_h^0$.

2.1. A posteriori error analysis

We start by introducing some notation. For any $K \in \mathcal{M}_h$, h_K stands for its diameter. Let $\mathcal{B}_h$ be the set of interior sides of the mesh $\mathcal{M}_h$. For any $e \in \mathcal{B}_h$, we denote h_e its diameter and Ω_e the collection of two elements sharing the common side e. For any element K, we denote ω_K the set of all elements in $\mathcal{M}_h$ that have non-empty intersection with K. For any side $e \in \mathcal{B}_h$ which is a common side of K_1 and K_2, ω_e denotes the union of ω_{K_1} and ω_{K_2}.

We now introduce the local error indicator η_K. For the non-interface elements $K \in \mathcal{M}_h \setminus \mathcal{M}_h^*$,

$$\eta_K^2 = \Lambda_K \left\| h_K a_K^{-1/2} f \right\|_{L^2(K)}^2 + \sum_{e\subset\partial K} \Lambda_e \left\| h_e^{1/2} a_e^{-1/2} [\![a_h \nabla u_h \cdot \mathbf{n}]\!]_e \right\|_{L^2(e)}^2.$$

For the interface elements $K \in \mathcal{M}_h^*$,

$$\eta_K^2 = \Lambda_K \left\| h_K a_K^{-1/2} f \right\|_{L^2(K)}^2 + \sum_{e\subset\partial K} \Lambda_e \left\| h_e^{1/2} a_e^{-1/2} [\![a_h \nabla u_h \cdot \mathbf{n}]\!]_e \right\|_{L^2(e)}^2 + \| |a - a_K|^{1/2} \nabla u_h \|_{L^2(K)}^2.$$

Here $a_e = \max_{K\in\Omega_e} a_K$, $[\![a_h \nabla u_h \cdot \mathbf{n}]\!]_e$ is the jump of discrete flux across side e, and

$$\Lambda_K = \max_{K'\subset\omega_K} \frac{a_K}{a_{K'}}, \quad \Lambda_e = \max_{K\in\Omega_e} \Lambda_K.$$

We remark that Λ_K equals to 1 for elements away from the interface Γ. We notice that a new term $\| |a - a_K|^{1/2} \nabla u_h \|_{L^2(K)}^2$ is introduced in the a posteriori error indicator for interface elements K. This term controls the error due to the approximation of coefficient $a(x)$ by $a_h(x)$.

Theorem 1. *Let u and u_h be the solution of (3) and (4), respectively. There exists a constant $C > 0$ depending only on the minimum angle of $\mathcal{M}_h$ such that*

$$|||u - u_h|||_\Omega \leqslant C \left(\sum_{K\in\mathcal{M}_h} \eta_K^2 \right)^{1/2},$$

where $|||\cdot|||_G = \sqrt{(a\nabla\phi, \nabla\phi)_G}$ is the energy norm on the domain $G \subset \mathbb{R}^2$.

Proof. First we know from Clément [10] that for any $\phi \in H_0^1(\Omega)$, we can define an interpolant $r_h\phi \in V_h^0$ such that there is a constant $C > 0$ depending only on the minimum angle of $\mathcal{M}_h$

$$\|\phi - r_h\phi\|_{L^2(K)} \leqslant C h_K \|\nabla\phi\|_{L^2(\omega_K)} \quad \forall K \in \mathcal{M}_h, \tag{5}$$

$$\|\phi - r_h\phi\|_{L^2(e)} \leqslant C h_e^{1/2} \|\nabla\phi\|_{L^2(\omega_e)} \quad \forall e \in \mathcal{B}_h. \tag{6}$$

Subtracting (4) from (3) and integrating by parts, we have, for any $\phi \in H_0^1(\Omega)$,

$$(a\nabla(u-u_h),\nabla\phi) = (f,\phi - r_h\phi) - (a_h\nabla u_h,\nabla(\phi - r_h\phi)) + ((a_h-a)\nabla u_h,\nabla\phi)$$
$$= \sum_{K\in\mathcal{M}_h}(f,\phi-r_h\phi)_K + \sum_{e\in\mathcal{B}_h}\int_e [[a_h\nabla u_h\cdot\mathbf{n}]]_e(\phi-r_h\phi)\mathrm{d}s + \sum_{K\in\mathcal{M}_h^*}((a_K-a)\nabla u_h,\nabla\phi)_K. \quad (7)$$

Using (5) we have

$$(f,\phi-r_h\phi)_K \leqslant \|f\|_{L^2(K)}\|\phi-r_h\phi\|_{L^2(K)} \leqslant C\Lambda_K^{1/2}\left\|h_K a_K^{-1/2} f\right\|_{L^2(K)}(a\nabla\phi,\nabla\phi)_{\omega_K}^{1/2} \leqslant C\Lambda_K^{1/2}\left\|h_K a_K^{-1/2} f\right\|_{L^2(K)}|||\phi|||_{\omega_K}.$$

Similarly, using (6) we can get

$$\int_e [\![a_h\nabla u_h\cdot\mathbf{n}]\!]_e(\phi-r_h\phi)\,\mathrm{d}s \leqslant C\Lambda_e^{1/2}\left\|h_e^{1/2}a_e^{-1/2}[\![a_h\nabla u_h\cdot\mathbf{n}]\!]_e\right\|_{L^2(e)}|||\phi|||_{\omega_e}.$$

The third term in (7) which is due to the non-body-fitted mesh can be estimated on each interface element $K\in\mathcal{M}_h^*$ as

$$((a_K-a)\nabla u_h,\nabla\phi)_K \leqslant \||a_K-a|^{1/2}\nabla u_h\|_{L^2(K)}\||a_K-a|^{1/2}\nabla\phi\|_{L^2(K)} \leqslant \||a_K-a|^{1/2}\nabla u_h\|_{L^2(K)}|||\phi|||_K.$$

This completes the proof by collecting above estimates. □

To conclude this subsection we describe briefly how the method can be extended for solving interface problems with non-homogeneous jump conditions. We also refer to Gong et al. [12] for related studies. Let $g\in H^2(\Gamma)$. We consider the model problem (1) with jump conditions

$$[\![u]\!]_\Gamma = 0, \quad \left[\!\left[a(x)\frac{\partial u}{\partial\mathbf{n}}\right]\!\right]_\Gamma = g \quad \text{on } \Gamma.$$

The weak formulation reads as: find $u\in H_0^1(\Omega)$ such that

$$\int_\Omega a(x)\nabla u\cdot\nabla v\,\mathrm{d}x = \int_\Omega fv\,\mathrm{d}x + \int_\Gamma gv\,\mathrm{d}s \quad \forall v\in H_0^1(\Omega). \quad (8)$$

To discretize the weak problem (8), we need a piecewise linear approximation Γ_h of Γ whose vertices are the intersection of the sides of the interface elements with Γ. Let g_h be the piecewise linear interpolation of g on Γ_h. The discrete problem is then to find $u_h\in V_h^0$ such that

$$\int_\Omega a_h(x)\nabla u_h\cdot\nabla v_h\,\mathrm{d}x = \int_\Omega fv_h\,\mathrm{d}x + \int_{\Gamma_h} g_h v_h\,\mathrm{d}s \quad \forall v_h\in V_h^0. \quad (9)$$

Let $\Gamma_h = \cup_{j=1}^{m_h} S_j^h$ and $\Gamma = \cup_{j=1}^{m_h} S_j$, where $S_j^h = K_j\cap\Gamma_h$ and $S_j = K_j\cap\Gamma$ for some $K_j\in\mathcal{M}_h^*$. For each K_j, a local coordinate system (s,t) can be defined so that S_j^h is the s axis and S_j is parameterized locally as $x(s),\ 0<s<h_j$, where h_j is the length of S_j^h. Assuming Γ is piecewise smooth so that each S_j is of class C^2, by the construction of Γ_h, we have $x(0)=x(h_j)=0$ and $x(s)\leqslant Ch_j^2,\ x'(s)\leqslant Ch_j,\ s\in[0,h_j]$.

To derive the a posteriori error estimate, we need to estimate the new term

$$\left|\int_\Gamma g\phi\,\mathrm{d}s - \int_{\Gamma_h} g_h\phi\,\mathrm{d}s\right| = \left|\int_\Gamma (g-g_h)\phi\,\mathrm{d}s + \int_\Gamma g_h\phi\,\mathrm{d}s - \int_{\Gamma_h} g_h\phi\,\mathrm{d}s\right| \leqslant C\|g-g_h\|_{L^2(\Gamma)}\|\phi\|_{H^1(\Omega)} + \left|\int_\Gamma g_h\phi\,\mathrm{d}s - \int_{\Gamma_h} g_h\phi\,\mathrm{d}s\right|,$$

where g_h is extended on Γ by using the local coordinates as $g_h(s,x(s)) = g_h(s,0)$. The second term can be estimated using the method in [8, Lemma 2.2] as

$$\left|\int_\Gamma g_h\phi\,\mathrm{d}s - \int_{\Gamma_h} g_h\phi\,\mathrm{d}s\right| \leqslant C\sum_{K\in\mathcal{M}_h^*} h_K\|g_h\|_{L^2(\Gamma_h\cap K)}\|\phi\|_{H^1(K)}.$$

The a posteriori error estimate can then be derived by using the same method as in Theorem 1. Here we omit the details.

2.2. Adaptive algorithm and numerical results

The implementation of our 2D adaptive algorithm is based on the adaptive finite element package ALBERTA [21] and is carried out on SGI Origin 3800. We first describe the 2D adaptive algorithm.

Algorithm 1. Given a tolerance TOL > 0. Generate an initial mesh $\mathcal{M}_0$.

- Solve the discrete problem (4) on $\mathcal{M}_0$;
- Compute the local error indicator η_K on each $K\in\mathcal{M}_0$;
- Set $k=0$;

- While $\mathcal{E}_k = \left(\sum_{K\in\mathcal{M}_k}\eta_K^2\right)^{1/2} > \mathrm{TOL}$, do
  - Refine all $K \in \mathcal{M}_k$ satisfying $\eta_K > \frac{1}{2}\max_{K\in\mathcal{M}_k}\eta_K$ to construct a conforming mesh $\mathcal{M}_{k+1}$;
  - Solve the discrete problem (4) on $\mathcal{M}_{k+1}$;
  - Compute the local error indicator η_K on each $K \in \mathcal{M}_{k+1}$;
  - Set $k = k+1$.

  End while

Now we present several numerical examples to demonstrate the efficiency of the proposed algorithm. The discrete system of linear equations is solved by preconditioned CG method with diagonal preconditioning.

Example 1. Let $\Omega = (-2,2)^2$ and the interface Γ is a unit circle centered at the origin. f is determined from the following exact solution which is given in polar coordinates

$$u(r) = \begin{cases} e^{r^2-1} + R - 1 & \text{if } r \leqslant 1, \\ Rr^2 & \text{if } r > 1. \end{cases}$$

The coefficient $a(x)$ equals to R or 1 depending x is inside or outside the unit circle. With this example we want to test the robustness of our a posteriori error estimate with respect to the contrast of coefficients.

In Table 1, we show the number of adaptive iterations k, the number of degrees of freedom N_k, and the effectivity index for different values of R. The energy error $|||u-u_k|||_\Omega$ is computed through the following formula:

$$|||u-u_k|||_\Omega^2 = \int_\Omega f(u-2u_k)\mathrm{d}x + \int_{\partial\Omega}(a(x)\nabla u\cdot\mathbf{n})(u-2u_k)\mathrm{d}s + |||u_k|||_\Omega^2.$$

We observe that the effectivity index $|||u-u_k|||_\Omega/\mathcal{E}_k$ is moderate even when R is fairly large, which shows our a posteriori error estimator does not underestimate the error introduced by the pollution effects of high contrast of coefficients. Fig. 2 displays the surface plots of the exact solution u and the numerical solution u_k when $R = 50$ and $k = 10$. The corresponding adaptively refined mesh is displayed in Fig. 3.

From the $\log\mathcal{E}_k - \log N_k$ curves in Fig. 4, we observe that the associated numerical complexity is quasi-optimal: $|||u-u_k|||_\Omega \approx C\, N_k^{-1/2}$ is valid asymptotically.

Example 2. We consider an interface problem involving a sharp-edged interface. Γ consists of two parts Γ_1 and Γ_2, where

$$\Gamma_1: \quad (x_1-2)^2 + \left(x_2 - \frac{19}{6}\right)^2 = \left(\frac{25}{6}\right)^2, \quad \Gamma_2: \quad (x_1-2)^2 + \left(x_2 + \frac{19}{6}\right)^2 = \left(\frac{25}{6}\right)^2.$$

Table 1
The performance of the AIIFEM algorithm and the error indicator $\mathcal{E}_k$ (Example 1).

R	k	N_k	$\|\|\|u-u_k\|\|\|_\Omega/\mathcal{E}_k$
5	14	1,077,621	0.31
50	18	939,861	0.54
500	18	710,285	0.59
5000	19	1,089,153	0.62

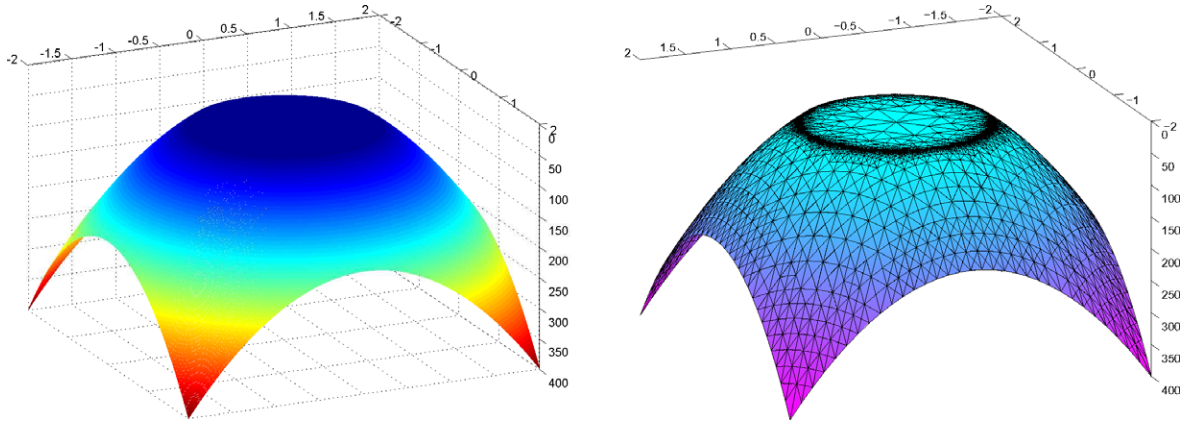

Fig. 2. The surface plots of the exact solution u (left) and the numerical solution u_k when $R = 50$ and $k = 10$ (Example 1).

Γ_1 and Γ_2 intersect at a positive angle. Let $\Omega = (-2,2)^2$ (Fig. 5). As shown in the figure, we set $a(x) = R$ in the dark region, and 1 in the rest. We set the source $f = 1$. The solution of the interface problem is then singular.

Fig. 6 shows the $\log \mathcal{E}_k - \log N_k$ curves for different choices of R. It indicates the associated numerical complexity is quasi-optimal: $\mathcal{E}_k \approx C\, N_k^{-1/2}$ is validated asymptotically.

Fig. 7 shows an adaptive mesh of 21,659 nodes after 14 iterations when $R = 100$. We observe that the mesh is locally refined along the interface. The corresponding surface plot of the numerical solution u_{14} is given in Fig. 8.

Example 3. In this example the interface is of the twisted checkerboard shape, as shown in Fig. 5. Let $\Omega = (-1,1)^2$. As in Example 2, we set $a(x) = R$ in the dark region, and 1 in the rest. The source $f = 1$.

Fig. 9 shows the $\log \mathcal{E}_k - \log N_k$ curves which indicates that the adaptive meshes and the associated numerical complexity are quasi-optimal.

Fig. 10 shows an adaptively generated mesh when $R = 100$. We find the mesh away from the interface Γ is rather coarse because of different behaviors in the subdomains. Fig. 11 shows the corresponding surface plot of the numerical solution u_{12}.

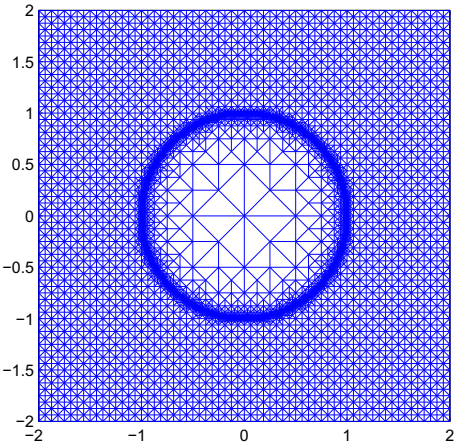

Fig. 3. The mesh of 18,541 degrees of freedom when $R = 50$ after 10 adaptive iterations (Example 1).

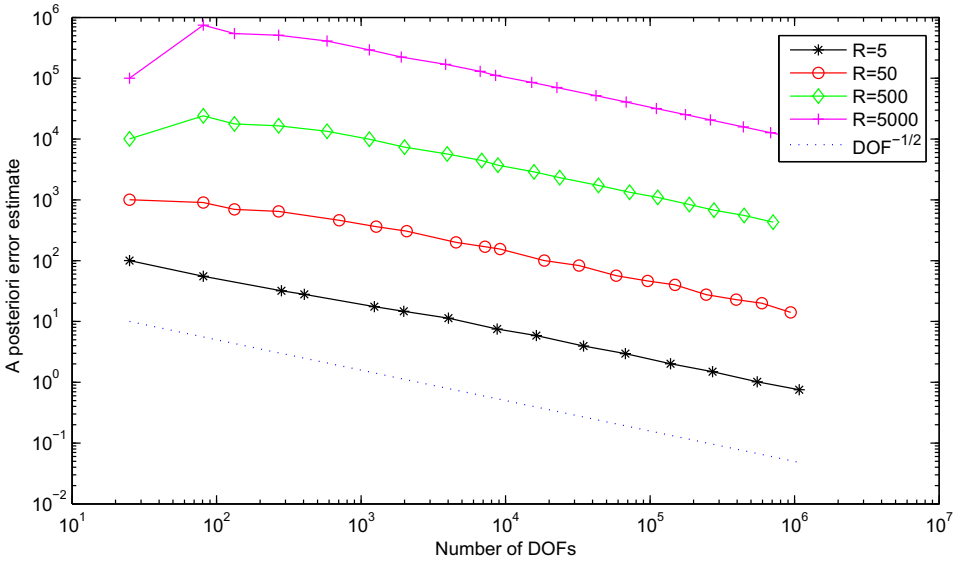

Fig. 4. The quasi-optimal convergence of the a posteriori error estimates for $R = 5, 50, 500, 5000$. The quasi-optimal decay is indicated by the line of slope $-1/2$ (Example 1).

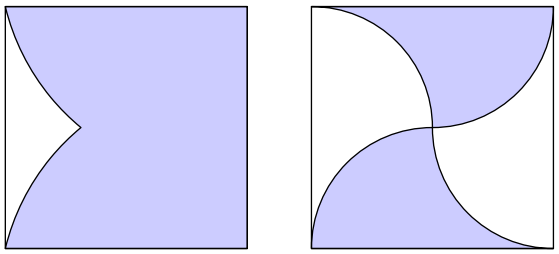

Fig. 5. The configuration of the interface used in Example 2 (left) and Example 3 (right).

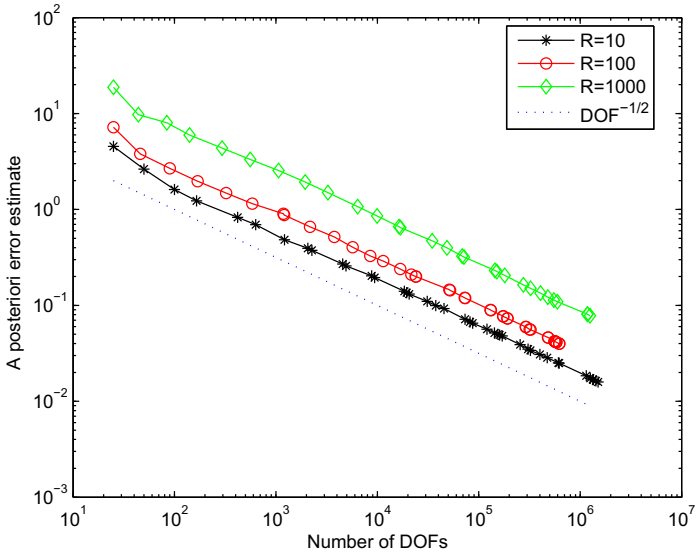

Fig. 6. The quasi-optimal convergence of the a posteriori error estimates for $R = 10, 100, 1000$. The quasi-optimal decay is indicated by the line of slope $-1/2$ (Example 2).

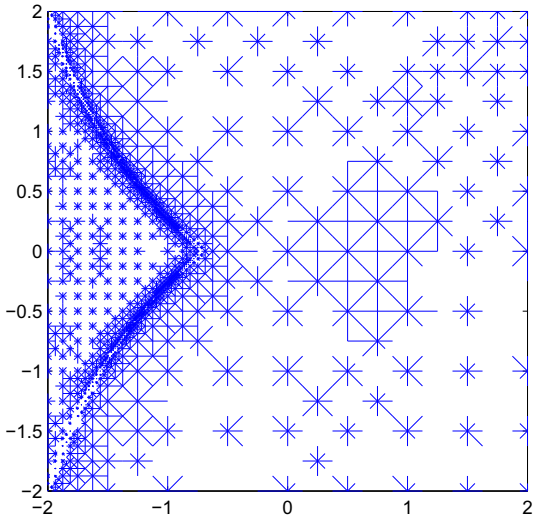

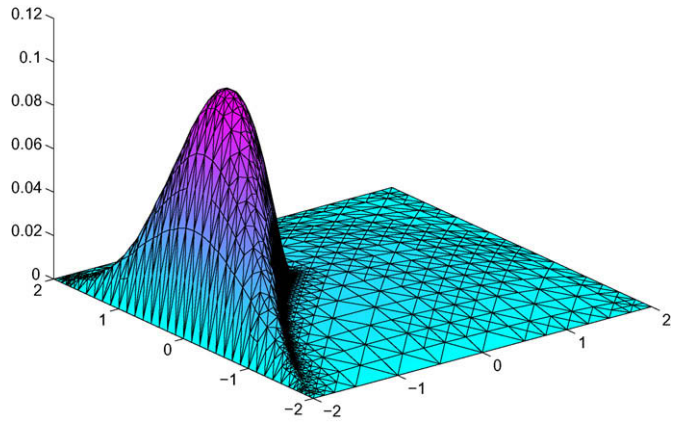

Fig. 8. The surface plot of the numerical solution u_k solved on the mesh of Fig. 7 when $R = 100$ and $k = 14$ (Example 2).

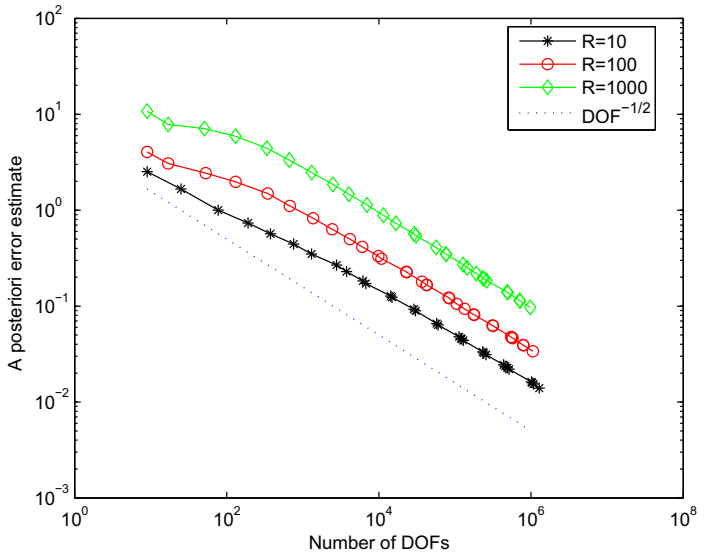

Fig. 9. The quasi-optimal convergence of the a posteriori error estimates for $R = 10, 100, 1000$. The quasi-optimal decay is indicated by the line of slope $-1/2$ (Example 3).

3. The 3D elliptic interface problem

In this section we extend the idea developed in Section 2 to solve 3D interface problems. Let Ω be a polyhedral domain in $\mathbb{R}^3$. Let $\mathcal{M}_h$ be a regular tetrahedral partition of the domain Ω. For any element $K \in \mathcal{M}_h^*$, the set of all elements that have non-empty intersection with the interface, we distinguish four cases of how Γ intersects with K:

(i) All four vertices lie in one of the two subdomains (Fig. 12(a)).
(ii) Three vertices $A_1,\ A_2,\ A_3$ lie in one subdomain, the forth vertex A_4 lies in the other subdomain, and Γ intersects each edge $A_1A_4,\ A_2A_4,\ A_3A_4$ at only one point (Fig. 12(b)).
(iii) Two vertices $A_1,\ A_2$ lie in one subdomain, the other two vertices $A_3,\ A_4$ lie in another subdomain, and Γ intersects each edge $A_1A_3,\ A_1A_4,\ A_2A_3,\ A_2A_4$ at only one point (Fig. 13(a)).
(iv) The four vertices do not lie in one subdomain and Γ intersects at least one edge of K whose vertices lie in different subdomains at more than one point (Fig. 13(b)).

We define the discrete coefficient function $a_h(x)$ as

$$a_h(x) = \begin{cases} a(x) & \text{if } x \in K,\ K \text{ non-interface element;} \\ a_K(x) & \text{if } x \in K,\ K \text{ interface element.} \end{cases} \tag{10}$$

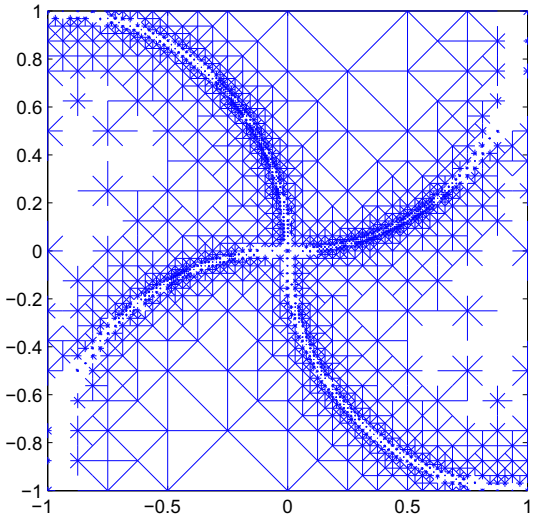

For each interface element $K \in \mathcal{M}_h^*,\ a_K(x)$ is defined according to the four cases as follows. In case (i) we define $a_K(x) = a_i$ if all four vertices lie in $\Omega_i,\ i = 1, 2$. In the cases (ii) and (iii) we first approximate the interface by plane patches connecting the

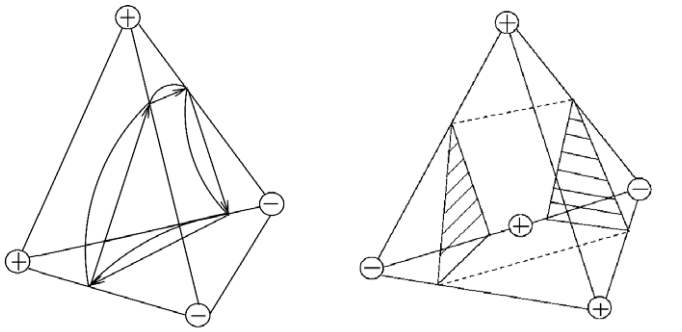

(a) The intersection is a curved quadrilateral.

(b) The intersection has multiple components.

Fig. 13. The intersection of Γ with the interface element K: case (iii) and case (iv).

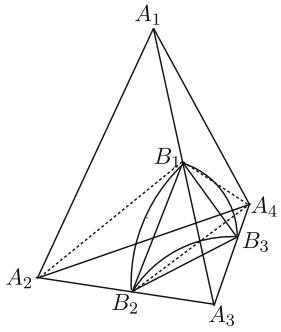

Fig. 14. Add new nodal points at intersections.

intersection points between the interface and the edges of K as illustrated in Figs. 12(b) and 13(a). The plane patches divide K into two parts K_1 and K_2 so that $K_i \subset \Omega_i$. For each part, we set $a_K(x) = a_i$ if that part lies in $\Omega_i,\ i = 1, 2$. In the exceptional case (iv) as illustrated in Fig. 13(b), we simply define $a_K(x) = \min_{x\in K} a(x)$.

To derive our discrete approximation to (3), we introduce an intermediate conforming mesh $\widehat{\mathcal{M}}_h$ which is the refinement of $\mathcal{M}_h$ by breaking each interface tetrahedra into several small tetrahedra as illustrated in Fig. 14 for case (ii). $\widehat{\mathcal{M}}_h$ is then a body-fitted mesh. Let $\widehat{V}_h$ be the H^1-conforming linear finite element space over $\widehat{\mathcal{M}}_h$. Set $\widehat{V}_h^0 = \widehat{V}_h \cap H_0^1(\Omega)$. The discrete problem is then to find $\hat{u}_h \in \widehat{V}_h^0$ such that

$$\int_\Omega a_h(x)\nabla\hat{u}_h \cdot \nabla v_h \,\mathrm{d}x = \int_\Omega f v_h \,\mathrm{d}x \quad \forall v_h \in \widehat{V}_h^0. \tag{11}$$

We note that the resulting linear system (11) is solved on the intermediate mesh $\widehat{\mathcal{M}}_h$. In the following, however, the a posteriori error estimate will be performed on $\mathcal{M}_h$, not $\widehat{\mathcal{M}}_h$. Moreover, $\mathcal{M}_h$ will be refined to produce the new mesh in the adaptive computations. In this way, the mesh quality will not deteriorate during the adaptive iterations if the newest vertex bisection algorithm is used to refine the meshes, see e.g. [4].

Now we derive the a posteriori error estimate for the discrete problem (11). For any $K \in \mathcal{M}_h$, we introduce the local error indicator η_K which is of the same form as in Section 2. For the non-interface elements $K \in \mathcal{M}_h \setminus \mathcal{M}_h^*$,

$$\eta_K^2 = \Lambda_K \left\| h_K a_K^{-1/2} f \right\|_{L^2(K)}^2 + \sum_{e\subset K} \left\| h_e^{1/2} a_e^{-1/2} [\![a_h \nabla\hat{u}_h \cdot \mathbf{n}]\!]_e \right\|_{L^2(e)}^2.$$

For the interface elements $K \in \mathcal{M}_h^*$,

$$\eta_K^2 = \left\| h_K a_K^{-1/2} f \right\|_{L^2(K)}^2 + \sum_{e\subset K} \left\| h_e^{1/2} a_e^{-1/2} [\![a_h \nabla\hat{u}_h \cdot \mathbf{n}]\!]_e \right\|_{L^2(e)}^2 + \| |a - a_h|^{1/2} \nabla\hat{u}_h \|_{L^2(K)}^2.$$

Here $a_e = \max_{K\in\Omega_e} a_K$, and $[\![a_h \nabla\hat{u}_h \cdot \mathbf{n}]\!]_e$ is the jump of flux across side e, and

$$\Lambda_K = \max_{K'\subset\omega_K} \frac{a_K}{a_{K'}}, \quad \Lambda_e = \max_{K\in\Omega_e} \Lambda_K.$$

Let V_h be the H^1-conforming linear finite element space over the mesh $\mathcal{M}_h$. Since $\widehat{\mathcal{M}}_h$ is a refinement of $\mathcal{M}_h$, $V_h \subset \widehat{V}_h$. The following theorem can be proved by the same method as in the proof of Theorem 1 by using the Clément interpolant in V_h. Here we omit the details.

Theorem 2. *Let u and $\hat{u}_h$ be the solution of (3) and (11), respectively. There exists a constant $C > 0$ depending only on the minimum angle of $\mathcal{M}_h$ such that*

$$|||u - \hat{u}_h|||_\Omega \leqslant C\left(\sum_{K\in\mathcal{M}_h} \eta_K^2\right)^{1/2},$$

where $|||\cdot|||_G = \sqrt{(a\nabla\phi, \nabla\phi)_G}$ is the energy norm on the domain $G \subset \mathbb{R}^3$.

3.1. Adaptive algorithm and numerical experiments

The implementation of our 3D AIIFEM method is based on the parallel adaptive finite element package PHG [22,23]. The computation is carried out on LSSC-II in the State Key Laboratory on Scientific and Engineering Computing of Chinese Academy of Sciences.

Algorithm 2. Given tolerance TOL > 0.

- Generate an initial mesh $\mathcal{M}_0$, $k = 0$;
- While $\mathcal{E}_k = \left(\sum_{K\in\mathcal{M}_k} \eta_K^2\right)^{1/2} >$ TOL, do
  - Designate the discrete coefficient function a_k on $\mathcal{M}_k$;
  - Add new elements in interface elements to generate an intermediate conforming mesh $\widehat{\mathcal{M}}_k$;
  - Solve the discrete problem on $\widehat{\mathcal{M}}_k$;
  - Compute the local error indicator η_K on each $K \in \mathcal{M}_k$;
  - Refine all $K \in \mathcal{M}_k$ satisfying $\eta_K > \frac{1}{2}\max_{K\in\mathcal{M}_k}\eta_K$ to construct a conforming mesh $\mathcal{M}_{k+1}$;
  - Set $k = k + 1$.

  End while

Now we report several numerical experiments to demonstrate the competitive behavior of the algorithm. The discrete system of linear equations is solved by preconditioned CG method with diagonal preconditioning.

Example 4. Let $\Omega = (-2, 2)^3$ and the interface be a unit sphere centered at the origin. The exact solution is given in the spherical coordinates as

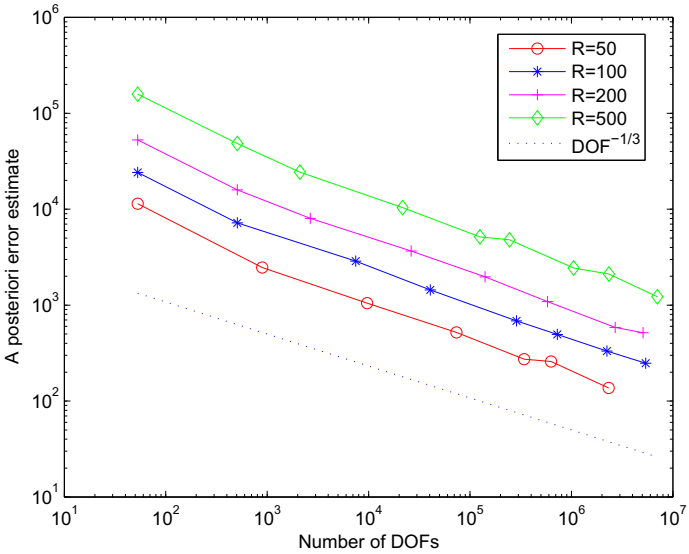

Fig. 15. The quasi-optimal convergence of the a posteriori error estimates for $R = 50, 100, 200, 500$. The quasi-optimal decay is indicated by the line of slope $-1/3$ (Example 4).

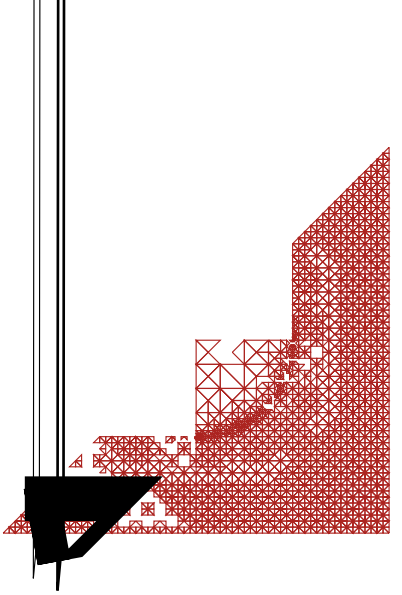

$$u(r) = \begin{cases} e^{r^2-1} + R - 1 & \text{if } r \leqslant 1; \\ Rr^2 & \text{if } r > 1. \end{cases}$$

We set the coefficient $a(x) = R$ inside the sphere and $a(x) = 1$ outside.

Fig. 15 shows the $\log \mathcal{E}_k - \log N_k$ curves for different values of R, where $\mathcal{E}_k$ is the a posteriori error estimate over $\mathcal{M}_k$ and N_k is the number of degrees of freedom. It indicates that the adaptive meshes and the associated computational complexity are quasi-optimal: $\mathcal{E}_k = CN_k^{-1/3}$ is valid asymptotically. Fig. 16 shows an adaptive mesh using 407,559 degrees of freedom when $R = 50$.

Example 5. In this example we consider an elliptic problem involving an interface having cusps (see Fig. 17). We set the computational domain $\Omega = (-2, 2)^3$, $\Omega_1 = \{x = (x_1, x_2, x_3)^T : \ x_1 > 0.1, \ x_2 > 0.1, \ x \in S_1 \setminus S_2\}$, where S_1 and S_2 are two ellipsoids defined by

$$S_1 : \quad \frac{(x_1 - 0.1)^2}{1.5^2} + \frac{(x_2 - 0.1)^2}{1.2^2} + (x_3 - 0.1)^2 < 1,$$

and

$$S_2 : \quad (x_1 - 0.1)^2 + (x_2 - 0.1)^2 + (x_3 - 0.1)^2 \leqslant 1.$$

Note that the interface $\Gamma = \partial\Omega_1$ is not even Lipschitz continuous and has the singularity at the cusp points $(0.1, 0.1, \pm 1.1)$. We set $a(x) = R$ in Ω_1, $a(x) = 1$ in Ω_2, and $f = 1$ in Ω.

Fig. 18 shows the $\log \mathcal{E}_k - \log N_k$ curves for different values of R. It indicates that the algorithm achieves the quasi-optimal convergence of the a posteriori error estimates in terms of the number of degrees of freedom. Fig. 19 shows a slice of adaptive mesh using 670,372 nodes when $R = 50$ at the plane $x_1 - x_2 = 0$. We observe the mesh is locally refined near the cusp points. Fig. 20 shows the surface plot of numerical solution u_{20} for $R = 10$.

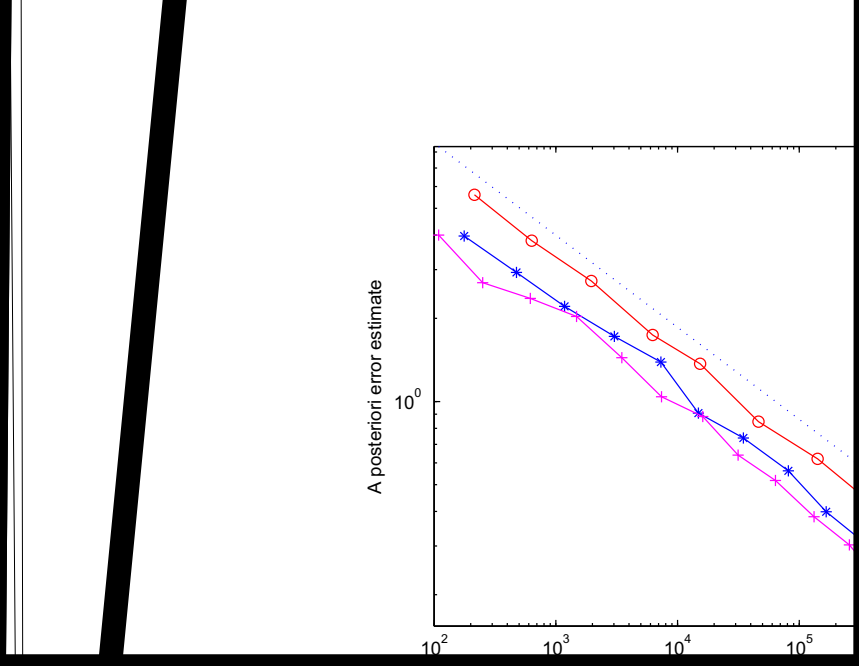
A posteriori error estimate
10^0
10^2
10^3
10^4
10^5

4. The Maxwell interface problem

Let Ω be a polyhedral domain in $\mathbb{R}^3$ with boundary Σ. Let Ω_1 be a subdomain in Ω with boundary Γ and $\Omega_2 = \Omega \setminus \overline{\Omega}_1$. We consider in this section the following Maxwell interface problem

$$\nabla \times (\mu(x)^{-1}\nabla \times \mathbf{E}) - \kappa^2 \varepsilon(x)\mathbf{E} = \mathbf{f} \quad \text{in } \Omega, \tag{12}$$

$$[\![\mathbf{n} \times \mathbf{E}]\!]_\Gamma = 0, \quad [\![\mathbf{n} \times \mu(x)^{-1}(\nabla \times \mathbf{E})]\!]_\Gamma = 0, \quad [\![\mathbf{n} \cdot \kappa^2 \varepsilon(x)\mathbf{E}]\!]_\Gamma = 0 \quad \text{on } \Gamma \tag{13}$$

with the impedance boundary condition on Σ

$$\mu^{-1}(\nabla \times \mathbf{E}) \times \mathbf{n} - \mathbf{i}\kappa \mathbf{E}_t = \mathbf{g} \quad \text{on } \Sigma, \quad \mathbf{E}_t = \mathbf{n} \times \mathbf{E} \times \mathbf{n}. \tag{14}$$

$\mathbf{E}$ is the time-harmonic electric field. ε is the complex relative dielectric coefficient, $\mu > 0$ is the relative magnetic permeability, $\kappa > 0$ is the wave number. We assume $\mu(x)$ and $\varepsilon(x)$ are constant in each of the subdomains: $\mu(x) = \mu_i,\ \varepsilon(x) = \varepsilon_i$ for $x \in \Omega_i,\ i = 1, 2$. $\mathbf{f}$ is the source associated with the applied current density and $\mathbf{g}$ is determined from the incidence field.

Let $\mathbf{f} \in L^2(\Omega)^3$ and $\mathbf{g} \in L^2(\Sigma)^3$ satisfying $\mathbf{g} \cdot \mathbf{n} = 0$ on Σ. Denote $\mathbf{U}$ the subspace of $H(\mathrm{curl}; \Omega)$

$$\mathbf{U} = \{\mathbf{v} \in H(\mathrm{curl}; \Omega) : \mathbf{v}_t \in L^2(\Sigma)^3\},$$

which is equipped with the graph norm

$$\|\mathbf{v}\|_{\mathbf{U}} = (\|\mathbf{v}\|^2_{H(\mathrm{curl};\Omega)} + \|\mathbf{v}_t\|^2_{L^2(\Sigma)})^{1/2}.$$

The weak formulation of the problem (12)–(14) is then to find $\mathbf{E} \in \mathbf{U}$ such that

$$b(\mathbf{E}, \mathbf{v}) = (\mathbf{f}, \mathbf{v}) + \langle \mathbf{g}, \mathbf{v}_t \rangle_\Sigma \quad \forall \mathbf{v} \in \mathbf{U}, \tag{15}$$

where $\langle \cdot, \cdot \rangle_\Sigma$ is the inner product on $L^2(\Sigma)^3$, and

$$b(\mathbf{E}, \mathbf{v}) := (\mu^{-1}\nabla \times \mathbf{E}, \nabla \times \mathbf{v}) - \kappa^2(\varepsilon \mathbf{E}, \mathbf{v}) - \mathbf{i}\kappa \langle \mathbf{E}_t, \mathbf{v}_t \rangle_\Sigma.$$

The existence and uniqueness of the solution of (15) under various conditions on the domain Ω and the coefficients have been studied in [19]. Here for the sake of simplicity, we assume that problem (15) has a unique solution. Then the general theory in Babuška and Aziz [2, Chap. 5] implies that there exists a constant $\gamma > 0$ depending only on the domain Ω and the coefficients $\mu,\ \varepsilon,\ \kappa$ such that

$$\sup_{0 \neq \mathbf{v} \in \mathbf{U}} \frac{|b(\mathbf{u}, \mathbf{v})|}{\|\mathbf{v}\|_{\mathbf{U}}} \geqslant \gamma \|\mathbf{u}\|_{\mathbf{U}} \quad \forall \mathbf{u} \in \mathbf{U}. \tag{16}$$

Let $\mathcal{M}_h$ be a regular tetrahedral partition of the domain Ω. We define the discrete coefficients $\mu_h(x)$ and $\varepsilon_h(x)$ over the mesh $\mathcal{M}_h$ from $\mu(x)$ and $\varepsilon(x)$ as the definition of $a_h(x)$ in (10). Let $\widehat{\mathcal{M}}_h$ be the intermediate mesh obtained from $\mathcal{M}_h$ as in Section 3. We make use of the lowest order Nédélec edge element $\widehat{\mathbf{U}}_h$ over the mesh $\widehat{\mathcal{M}}_h$

$$\widehat{\mathbf{U}}_h = \{\mathbf{v}_h \in H(\mathrm{curl}; \Omega) : \mathbf{v}_h|_K = \mathbf{a}_K + \mathbf{b}_K \times x\ \forall \mathbf{a}_K,\ \mathbf{b}_K \in \mathbb{R}^3,\ \forall K \in \widehat{\mathcal{M}}_h\}.$$

The discrete problem is then to find $\mathbf{E}_h \in \widehat{\mathbf{U}}_h$ such that

$$b_h(\mathbf{E}_h, \mathbf{v}_h) = (\mathbf{f}, \mathbf{v}_h) + \langle \mathbf{g}, \mathbf{v}_{h,t} \rangle_\Sigma \quad \forall \mathbf{v}_h \in \widehat{\mathbf{U}}_h, \tag{17}$$

where

$$b_h(\mathbf{E}_h, \mathbf{v}_h) = (\mu_h^{-1}\nabla \times \mathbf{E}_h, \nabla \times \mathbf{v}_h) - \kappa^2(\varepsilon_h \mathbf{E}_h, \mathbf{v}_h) - \mathbf{i}\kappa \langle \mathbf{E}_{h,t}, \mathbf{v}_{h,t} \rangle_\Sigma.$$

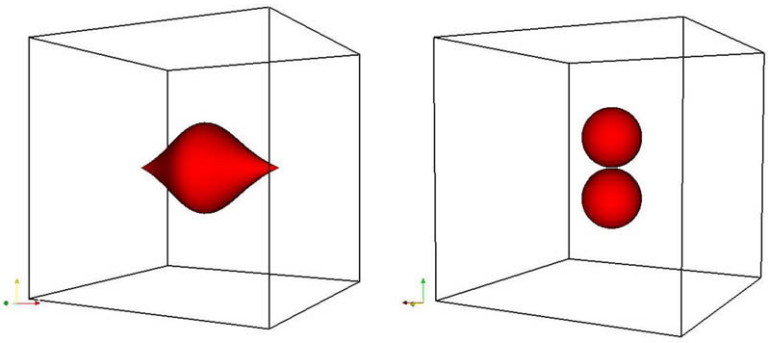

Fig. 21. The configuration of the interface used in Example 6 (left) and 7 (right).

The local error indicator η_K is defined as

$$\begin{aligned}\eta_K^2 = {} & h_K^2 \|\mathbf{f} + \kappa^2 \varepsilon_h \mathbf{E}_h - \nabla \times (\mu_h^{-1} \nabla \times \mathbf{E}_h)\|_{L^2(K)}^2 + h_K^2 \|\operatorname{div}(\mathbf{f} + \kappa^2 \varepsilon_h \mathbf{E}_h)\|_{L^2(K)}^2 \\ & + \delta_K \left(\left\| |\mu^{-1} - \mu_h^{-1}|^{1/2} \nabla \times \mathbf{E}_h \right\|_{L^2(K)}^2 + \|\kappa |\varepsilon - \varepsilon_h|^{1/2} \mathbf{E}_h\|_{L^2(K)}^2 \right) \\ & + \sum_{e \subset \partial K, e \not\subset \Sigma} h_e \left(\| [\![\mu_h^{-1} \nabla \times \mathbf{E}_h \times \mathbf{n}]\!]_e \|_{L^2(e)}^2 + \| [\![(\mathbf{f} + \kappa^2 \varepsilon_h \mathbf{E}_h) \cdot \mathbf{n}]\!]_e \|_{L^2(e)}^2 \right) + \sum_{e \subset \partial K, e \subset \Sigma} h_e \left\| \mu_h^{-1} \nabla \times \mathbf{E}_h \times \mathbf{n} - \mathbf{i}\kappa \mathbf{E}_{h,t} - \mathbf{g} \right\|_{L^2(e)}^2 \\ & + \sum_{e \subset \partial K, e \subset \Sigma} h_e \| \operatorname{div}_\Sigma (\mathbf{g} + \mathbf{i}\kappa \mathbf{E}_{h,t}) - (\mathbf{f} + \kappa^2 \varepsilon_h \mathbf{E}_h) \cdot \mathbf{n} \|_{L^2(e)}^2 .\end{aligned}$$

Here $\delta_K = 1$ if K is an interface element, and $\delta_K = 0$ otherwise. The surface divergence $\operatorname{div}_\Sigma$ on Σ is defined as the conjugate operator of the surface gradient $\nabla_\Sigma = \mathbf{n} \times \nabla \times \mathbf{n}$ with respect to the inner product $\langle \cdot, \cdot \rangle_\Sigma$. We refer to [19] for details.

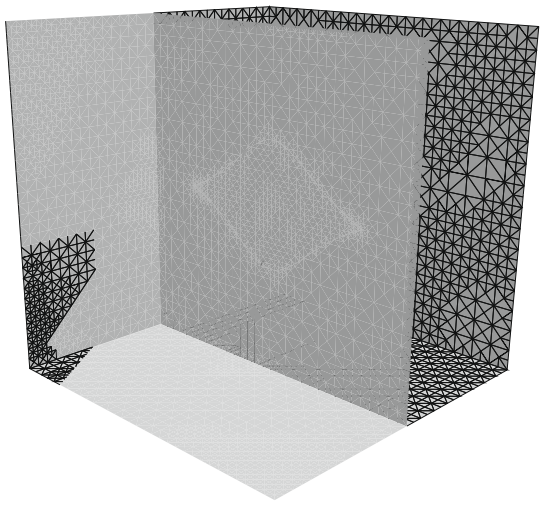

Theorem 3. *Let* $\mathbf{E}$ *and* $\mathbf{E}_h$ *be the solutions of (15) and (17), respectively. Then there exists a constant C depending only on the minimum angle of the mesh so that*

$$\|\mathbf{E}-\mathbf{E}_h\|_{\mathbf{U}} \leqslant C\gamma^{-1}\left(\sum_{K\in\mathcal{M}_h}\eta_K^2\right)^{1/2}.$$

Proof. The proof modifies the argument in [9]. We will use the regular decomposition of the vector field in $H(\mathrm{curl};\Omega)$ due to Birman and Solomyak [6] (see also [9]). For any $\mathbf{v}\in H(\mathrm{curl};\Omega)$, there exists a function $\mathbf{v}_s\in H^1(\Omega)^3\cap H(\mathrm{curl};\Omega)$ and $\phi\in H^1(\Omega)$ such that

$$\mathbf{v}=\mathbf{v}_s+\nabla\phi, \tag{18}$$

and

$$\|\mathbf{v}_s\|_{H^1(\Omega)}+\|\phi\|_{H^1(\Omega)}\leqslant C\|\mathbf{v}\|_{H(\mathrm{curl};\Omega)}. \tag{19}$$

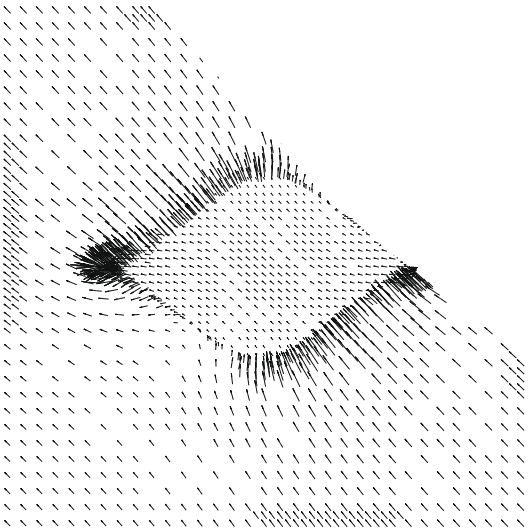

Let V_h be the piecewise linear H^1-conforming finite element space over $\mathcal{M}_h$, $\mathbf{U}_h$ the lowest order Nédélec edge element space over $\mathcal{M}_h$. We need the Clément interpolant $P_h : H^1(\Omega) \to V_h$ in [10] and the Beck–Hiptmair–Hoppe–Wohlmuth interpolant $\Pi_h : H^1(\Omega)^3 \cap H(\mathrm{curl};\Omega) \to \mathbf{U}_h$ in [5]. P_h and Π_h satisfy the following stability properties: For any element K and side e,

$$\|\phi - P_h\phi\|_{L^2(K)} \leqslant Ch_K\|\nabla\phi\|_{L^2(\omega_K)}, \quad \|\phi - P_h\phi\|_{L^2(e)} \leqslant Ch_e^{1/2}\|\nabla\phi\|_{L^2(\omega_e)}, \tag{20}$$

$$\|\mathbf{w} - \Pi_h\mathbf{w}\|_{L^2(K)} \leqslant Ch_K|\mathbf{w}|_{H^1(\omega_K)}, \quad \|\mathbf{w} - \Pi_h\mathbf{w}\|_{L^2(e)} \leqslant Ch_e^{1/2}|\mathbf{w}|_{H^1(\omega_e)}. \tag{21}$$

By (15) and (17), we deduce that for any $\mathbf{v} \in \mathbf{U}$, $\mathbf{v}_h \in \mathbf{U}_h$,

$$\begin{aligned} b(\mathbf{E} - \mathbf{E}_h, \mathbf{v}) &= (\mu^{-1}\nabla \times (\mathbf{E} - \mathbf{E}_h), \nabla \times \mathbf{v}) - \kappa^2(\varepsilon(\mathbf{E} - \mathbf{E}_h), \mathbf{v}) - \mathbf{i}\kappa\langle \mathbf{E}_t - \mathbf{E}_{h,t}, \mathbf{v}_t\rangle_\Sigma \\ &= (\mathbf{f}, \mathbf{v} - \mathbf{v}_h) + \langle \mathbf{g}, \mathbf{v}_t - \mathbf{v}_{h,t}\rangle - b_h(\mathbf{E}_h, \mathbf{v} - \mathbf{v}_h) - \sum_{K\in\mathcal{M}_h^*} \left((\mu^{-1} - \mu_h^{-1})\nabla \times \mathbf{E}_h, \nabla \times \mathbf{v}\right)_K + \sum_{K\in\mathcal{M}_h^*} \kappa^2((\varepsilon \\ &\quad - \varepsilon_h)\mathbf{E}_h, \mathbf{v})_K. \end{aligned}$$

Apply (18) to the test function $\mathbf{v} = \mathbf{v}_s + \nabla\phi$. Since $\Pi_h\mathbf{v}_s$ and $\nabla P_h\phi$ belong to $\mathbf{U}_h$, by taking $\mathbf{v}_h = \Pi_h\mathbf{v}_s + \nabla P_h\phi$ and integrating by parts, we have

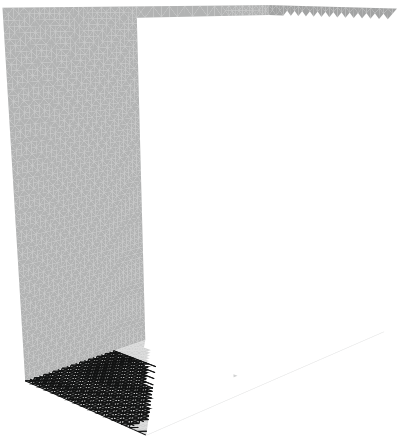

$$
\begin{aligned}
b(\mathbf{E}-\mathbf{E}_h,\mathbf{v}) &= \left(\mathbf{f}+\kappa^2\varepsilon_h\mathbf{E}_h-\nabla\times\left(\mu_h^{-1}\nabla\times\mathbf{E}_h\right),\mathbf{v}_s-\Pi_h\mathbf{v}_s\right)+\sum_{e\in\mathcal{B}_h}\int_e\left[\!\left[\mu_h^{-1}\nabla\times\mathbf{E}_h\times\mathbf{n}\right]\!\right]_e(\mathbf{v}_s-\Pi_h\mathbf{v}_s)\mathrm{d}s\\
&+\sum_{e\subset\Sigma}\int_e(\mathbf{g}+\mathbf{i}\kappa\mathbf{E}_{h,t}-\mu_h^{-1}\nabla\times\mathbf{E}_h\times\mathbf{n})(\mathbf{v}_s-\Pi_h\mathbf{v}_s)\mathrm{d}s-(\mathrm{div}(\mathbf{f}+\kappa^2\varepsilon_h\mathbf{E}_h),\phi-P_h\phi)\\
&+\sum_{e\in\mathcal{B}_h}\int_e[\![(\mathbf{f}+\kappa^2\varepsilon_h\mathbf{E}_h)\cdot\mathbf{n}]\!]_e(\phi-P_h\phi)\mathrm{d}s-\sum_{e\subset\Sigma}\int_e(\mathrm{div}_\Sigma(\mathbf{g}+\mathbf{i}\kappa\mathbf{E}_{h,t})-(\mathbf{f}+\kappa^2\varepsilon_h\mathbf{E}_h)\cdot\mathbf{n})(\phi-P_h\phi)\mathrm{d}s\\
&-\sum_{K\in\mathcal{M}_h^*}\left((\mu^{-1}-\mu_h^{-1})\nabla\times\mathbf{E}_h,\nabla\times\mathbf{v}\right)_K+\sum_{K\in\mathcal{M}_h^*}\kappa^2((\varepsilon-\varepsilon_h)\mathbf{E}_h,\mathbf{v})_K.
\end{aligned}
$$

By virtue of (19)–(21), we obtain easily

$$
b(\mathbf{E}-\mathbf{E}_h,\mathbf{v})\leqslant C\|\mathbf{v}\|_{\mathbf{H}(\mathrm{curl};\Omega)}\left(\sum_{K\in\mathcal{M}_k}\eta_K^2\right)^{\frac{1}{2}}\leqslant C\|\mathbf{v}\|_{\mathbf{U}}\left(\sum_{K\in\mathcal{M}_\|}\eta_K^2\right)^{\frac{1}{2}}.
$$

This completes the proof upon using the inf—sup condition (16). □

4.1. Numerical experiments

The discrete system of equations of (17) is not Hermitian and not positive definite. It is solved by the preconditioned MINRES method with AMS-PCG preconditioning as developed in [13].

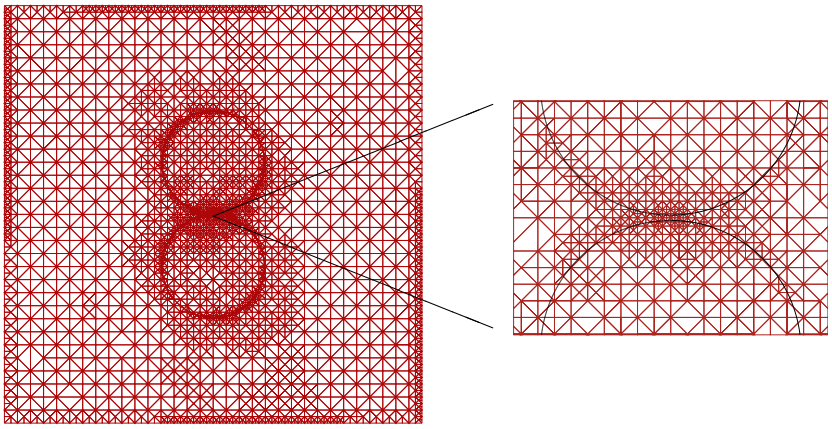

Fig. 28. The mesh at the plane of cross-section $x_2 = 0$ with a zoomed portion: 690,389 elements after 10 adaptive steps when $R = 10$ and $d = 0.02$. The part of interface is marked by the thick curve in the zoomed plot (Example 7).

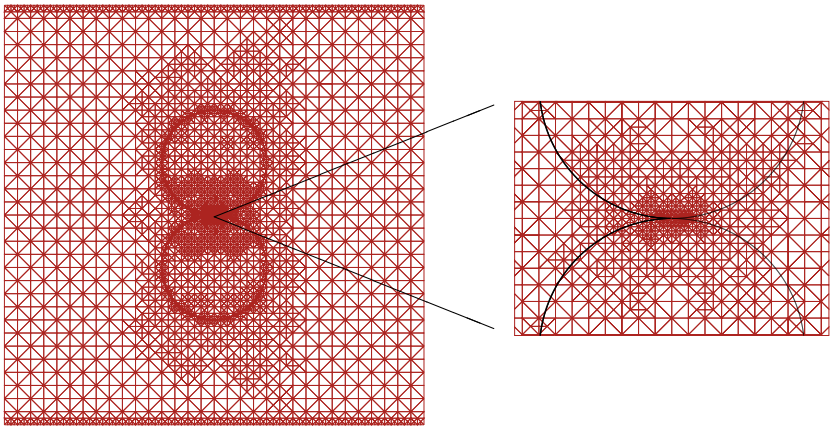

Fig. 29. The mesh at the plane of cross-section $x_1 = 0$ with a zoomed portion: 1,368,648 elements after 11 adaptive steps when $R = 10$ and $d = 0$. The part of interface is marked by the thick curve in the zoomed plot (Example 7).

Example 6. In this example the interface is given in the cylindrical coordinates as

$$x_1 = \frac{3}{4}\tan\theta, \quad \rho = \frac{3}{2}\cos\theta - \frac{3}{4}.$$

Let $\Omega = (-2,2)^3$. We set $\mu = 1,\ \kappa = 1$ in Ω and let the coefficient $\varepsilon(x)$ equal to R or 1 depending on whether x is inside or outside the spindle (see Fig. 21). The source and boundary terms are defined by

$$\mathbf{f} := \mathbf{0}, \quad \mathbf{g} := (\nabla \times \mathbf{E}_i) \times \mathbf{n} - \mathbf{i}\mathbf{E}_{i,t},$$

where the incident field $\mathbf{E}_i = (e^{\mathbf{i}x_2}, 0, e^{\mathbf{i}x_2})^T/\sqrt{2}$.

Fig. 22 shows the $\log \mathcal{E}_k - \log N_k$ curves for $R = 5, 10$ and it indicates that the adaptive meshes and the associated numerical complexity are quasi-optimal. In Fig. 23 we show the mesh after 9 adaptive steps when $R = 10$. We observe that the mesh is locally refined around the tips where the solution is singular. Fig. 24 shows the projection of real part of computed electric field on the plane of cross-section $x_2 = 0$ after 9 adaptive iterations for $R = 10$.

Example 7. In this example we assume the interfaces are two spherical surfaces that are very close to each other or touched (see Fig. 21). Let $\Omega = (-2,2)^3$. Set $\mu(x) = 1,\ \kappa = 1$ in Ω. Let $\varepsilon(x) = R$ inside each sphere with radius of 0.5 and $\varepsilon(x) = 1$ outside. The source and boundary terms are given by

$$\mathbf{f} := \mathbf{0}, \quad \mathbf{g} := (\nabla \times \mathbf{E}_i) \times \mathbf{n} - \mathbf{i}\mathbf{E}_{i,t},$$

where $\mathbf{E}_i = (e^{\mathbf{i}x_2}, 0, e^{\mathbf{i}x_2})^T/\sqrt{2}$. We note that the minimum distance between two interfaces, denoted by d, is small compared to the radius of the spheres.

Fig. 25 shows the $\log \mathcal{E}_k - \log N_k$ curves for different d with $R = 10$. It indicates that the associated numerical complexity is quasi-optimal. In Figs. 28 and 29 we show an adaptively generated mesh for $d = 0.02$ and $d = 0$, respectively (see Figs. 26 and 27 for a perspective view). The surface plots of corresponding L^2 norm of the real part of computed electric field are displayed in Fig. 30.

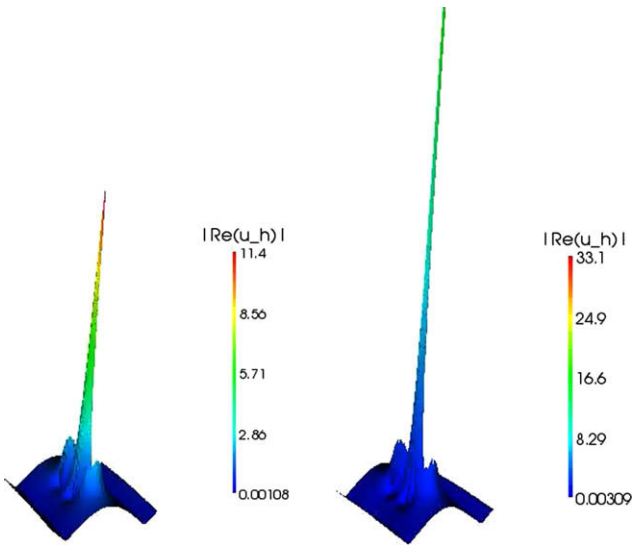

Fig. 30. The surface plot of L^2 norm of real part of computed electric field on the plane of cross-section $x_1 = 0$ for $d = 0.02$ (left) and $d = 0$ (right) when $R = 10$ (Example 7).

Table 2
The time (in s) and the memory allocation (in megabytes) in some adaptive steps when $R = 10$ and $d = 0$ (Example 7).

Number of elements	Linear system		Estimate	Refinement	Peak memory usage
	Assembly	Solution			
543,740	1.13	156.55	2.42	20.86	375.3
786,086	1.42	247.08	2.98	29.36	521.8
1,661,918	2.91	616.44	7.13	47.48	908.4
2,700,399	4.69	1033.77	14.75	71.57	974.1

In Table 2 we show the wall time used by various parts of our code and the memory allocated for the case when $d = 0$ with $R = 10$. The code is run with 80 processors. In the table, "Assembly", "Solution", "Estimate", and "Refinement", respectively, refer to the time used for assembling the discrete system, solving the discrete system, computing the a posteriori error estimates, and performing mesh refinements, while "Peak memory usage" refers to the largest memory used by each processor. We observe that most of the computing time is consumed by solving the discrete linear system of equations.

5. Concluding remarks

In this paper we developed an adaptive immersed interface finite element method for solving the elliptic and Maxwell interface problems. The finite element meshes that are adaptively refined according to local a posteriori error estimators need not fit with the interfaces. Our extensive numerical experiments indicate that the proposed algorithm can handle geometrically complicated interfaces that may have tips or cusps so that the exact solution of the problems may have strong singularities. We will extend the adaptive methods to solve time dependent problems involving moving interfaces.

Acknowledgment

The authors would like to thank the referee for the constructive comments that improved the presentation of the paper.

References

[1] I. Babuška, The finite element method for elliptic equations with discontinuous coefficients, Computing 5 (1970) 207–213.
[2] I. Babuška, A. Aziz, Survey lectures on mathematical foundations of the finite element method, in: A. Aziz (Ed.), The Mathematical Foundations of the Finite Element Method with Application to Partial Differential Equations, Academic Press, New York, 1973, pp. 5–359.
[3] I. Babuška, C. Rheinboldt, Error estimates for adaptive finite element computations, SIAM J. Numer. Anal. 15 (1978) 736–754.
[4] E. Bänsch, Local mesh refinement in 2 and 3 dimensions, Impact Comput. Sci. Eng. 3 (1991) 181C191.
[5] R. Beck, R. Hiptmair, R. Hoppe, B. Wohlmuth, Residual based a posteriori error estimators for eddy current computation, Math. Model. Numer. Anal. 34 (2000) 159–182.
[6] M.Sh. Birman, M.Z. Solomyak, L^2-Theory of the Maxwell operator in arbitrary domains, Uspekhi Mat. Nauk. 42 (1987) 61–76 (in Russian); Russian Math. Survey 43 (1987) 75–96 (in English).
[7] Z. Chen, S. Dai, On the efficiency of adaptive finite element methods for elliptic problems with discontinuous coefficients, SIAM J. Sci. Comput. 24 (2002) 443–462.
[8] Z. Chen, J. Zou, Finite element methods and their convergence for elliptic and parabolic interface problems, Numer. Math. 79 (1998) 175–202.
[9] Z. Chen, L. Wang, W. Zheng, An adaptive multilevel method for time-harmonic Maxwell equations with singularities, SIAM J. Sci. Comput. 29 (2007) 118–138.
[10] Ph. Clément, Approximation by finite element functions using local regularization, RAIRO Anal. Numer. 9 (1975) 77–84.
[11] M. Costabel, M. Dauge, S. Nicaise, Singularities of Maxwell interface problems, M^2AN Math. Model. Numer. Anal. 33 (1999) 627–649.
[12] Y. Gong, B. Li, Z. Li, Immersed-interface finite-element methods for elliptic interface problems with non-homogeneous jump conditions, SIAM J. Numer. Anal. 46 (2008) 472–495.
[13] R. Hiptmair, J. Xu, Nodal auxiliary space preconditioning in $H(\mathrm{curl})$ and $H(\mathrm{div})$ spaces, SIAM J. Numer. Anal. 45 (2007) 2483–2509.
[14] R. Kellogg, On the Poisson equation with intersecting interfaces, Appl. Anal. 4 (1974/1975) 101–129.
[15] R. LeVeque, Z. Li, The immersed interface method for elliptic equations with discontinuous coefficients and singular sources, SIAM J. Numer. Anal. 31 (1994) 1019–1044.
[16] Z. Li, K. Ito, the immersed interface method: numerical solutions of PDEs involving interfaces and irregular domains, SIAM (2006).
[17] Z. Li, T. Lin, X. Wu, New Cartesian grid methods for interface problems using the finite element formulation, Numer. Math. 96 (2003) 61–98.
[18] X. Liu, R.P. Fedkiw, M. Kang, A boundary condition capturing method for Poisson's equation on irregular domains, J. Comput. Phys. 160 (2000) 151–178.
[19] P. Monk, Finite Elements Methods for Maxwell Equations, Oxford University Press, 2003.
[20] C.S. Peskin, Numerical analysis of blood flow in heart, J. Comput. Phys. 25 (1977) 220–252.
[21] A. Schmidt, K.G. Siebert, Design of Adaptive Finite Element Software: The Finite Element Toolbox ALBERTA, Springer, 2005.
[22] L. Zhang, PHG: Parallel Hierarchical Grid, State Key Laboratory of Scientific and Engineering Computing of Chinese Academy of Sciences, 2007. <http://lsec.cc.ac.cn/phg/>.
[23] L. Zhang, A parallel algorithm for adaptive local refinement of tetrahedral meshes using bisection, Numer. Math.: Theor. Method Appl. 2 (2009) 65–89.